Wąsik, P., Seddon, A. M., Wu, H., & Briscoe, W. (2019). Dendritic surface patterns from Bénard-Marangoni instabilities upon evaporation of a reactive ZnO nanofluid droplet: A fractal dimension analysis. *Journal of Colloid and Interface Science*, *536*, 493-498. https://doi.org/10.1016/j.jcis.2018.10.077

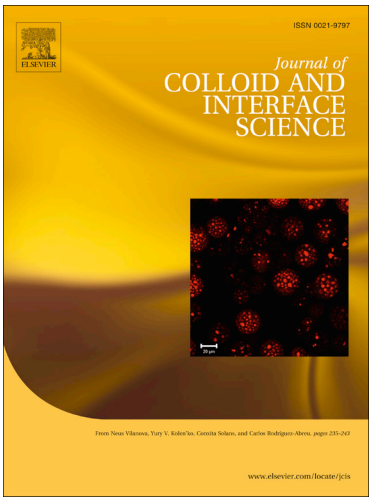


# Dendritic surface patterns from Bénard-Marangoni instabilities upon evaporation of a reactive ZnO nanofluid droplet: A fractal dimension analysis

Patryk Wąsik, Annela M. Seddon, Hua Wu, Wuge H. Briscoe

PII: S0021-9797(18)31277-3
DOI: https://doi.org/10.1016/j.jcis.2018.10.077
Reference: YJCIS 24232

To appear in: *Journal of Colloid and Interface Science*

Received Date: 30 July 2018
Revised Date: 23 October 2018
Accepted Date: 24 October 2018

Please cite this article as: P. Wąsik, A.M. Seddon, H. Wu, W.H. Briscoe, Dendritic surface patterns from Bénard-Marangoni instabilities upon evaporation of a reactive ZnO nanofluid droplet: A fractal dimension analysis, *Journal of Colloid and Interface Science* (2018), doi: https://doi.org/10.1016/j.jcis.2018.10.077

# Dendritic surface patterns from Bénard-Marangoni instabilities upon evaporation of a reactive ZnO nanofluid droplet: A fractal dimension analysis

**Patryk Wąsika,b, Annela M. Seddona,c, Hua Wub, and Wuge H. Briscoeb,***

**a Bristol Centre for Functional Nanomaterials (BCFN), HH Wills Physics Laboratory, University of Bristol, Tyndall Avenue, Bristol BS8 1TL, UK**

**b School of Chemistry, University of Bristol, Cantock's Close, Bristol BS8 1TS, UK**

**c School of Physics, HH Wills Physics Laboratory, Tyndall Avenue, University of Bristol, Bristol BS8 1TL, UK**

**Corresponding Author * E-mail: wuge.briscoe@bristol.ac.uk; Phone: +44 (0)117 3318256**

**Abstract**

We present a box counting fractal dimension (FD) analysis of the dendritic patterns obtained under conditions far from equilibrium *via* rapid evaporation of a sessile drop containing *reactive* ZnO nanoparticles. These dendrites were manifestations of solidified Bénard-Marangoni (BM) instability convection cells, and we previously noted that their complex hierarchical morphologies were superficially analogous to the foliage of red algae, Spanish dagger, or spider plant. The fractal dimension of the Bénard-Marangoni dendrites was found to vary in the range of 1.77 – 1.89 and also depend on the size of the Bénard-Marangoni cells. These fractal dimension results were correlated with the morphological details of the Bénard-Marangoni cells and ZnO particle characteristics, providing a quantitative description of such complex surface patterns emerging from the dynamic process of the Bénard-Marangoni instability.

**Keywords**

Evaporation Induced Self-Assembly, zinc oxide, evaporative drying, reactive nanofluids, Bénard-Marangoni instabilities, coffee ring effect, fractal dimension analysis.

Evaporation of a particle laden droplet represents a simple and versatile method to create intricate patterns and particle arrangements on surfaces over different length scales for device fabrication and surface modification – a process termed evaporation induced self-assembly (EISA) [1-2]. Most often, the dispersed particles are *inert*, and the residual pattern formation is determined by inter-particle forces and evaporation-induced solvent flows, which can be controlled by particle size, concentration, solvent composition or evaporation rate.

Our recent study on evaporation of *reactive* ZnO nanofluid sessile droplets [3] has shown that *in situ* generated molecular and particulate species could collude with and modify the solvent flow during evaporation *via* a mechanism different from that observed in the coffee ring effect [4], which would significantly affect the ultimate residual surface pattern. The mechanism is elucidated and described in some detail in Ref. [3]. In this process, the initial moisture-assisted dissolution of isobutylamine-coated ZnO nanoparticles was identified as a key step [5]. We have also shown that, by varying the morphology, size, and crystallinity of the ZnO particles, it is possible to control the dissolution of the ZnO nanocrystals, which would modify solvent flows and instabilities and in turn the morphology of the residual surface structures [6].

The EISA process based on reactive ZnO nano/microfluids can result in a plethora of hierarchical surface patterns composed of fibres or dendrites [3, 5-6]. For instance, the dendritic patterns triggered by Bénard-Marangoni (BM) instabilities [7-8] were analogous to the foliage of red algae, Spanish dagger, or spider plant [3]. To go beyond such a descriptive account and to seek understanding of the correlation between the surface pattern and the underpinning physical parameters, here we perform fractal dimension (FD) analysis of the surface patterns.

Fractal dimension analysis has evolved since the early work by Mandelbrot in 1982 [9], who described complex geometrical structures that imposed difficulties in representing their form using the classical Euclidean geometry. These irregular structures were called *fractals* and exhibited self-similarities, *i.e.* repetitions of complicated structures at many length scales [10]. Familiar theoretical fractal examples include a Cantor set, von Koch curves, and Sierpiński triangles defined by recursive algorithms that produce self-similar objects at different length scales at each iteration. Examples of natural fractals are also widespread, and fractal dimension analysis can be applied to these structures within a certain length scale range to yield the *fractal dimension* which can be considered a measure of "ruggedness", describing how a fractal structure scales with lengths when compared to classical geometric shapes. For instance, it has been applied to the analysis of the length of a coastline [11], the branching vascular tree in the human retina [12], cell shapes for cancer detection [13], diffusion limited particle aggregation [14], and patterns from chemical dissolutions [15]. The BM cellular pattern with dendritic microstructures we have observed from drying ZnO nano/microfluids exhibits complex hierarchical structures with various quasi-2D spatial arrangements, and thus represents a suitable candidate for the fractal dimension analysis.

Here, the analysis was performed on the residual patterns from evaporation of sessile drops containing three types of ZnO particles differing in size and shape: the in-house synthesised ZnO nanoparticles (*ca* 9 nm in size), and commercially acquired ZnO nanopowder (Sigma-Aldrich, <100 nm particle size, ~80% Zn basis), (*ca* 36-142 nm) and ZnO powder (Sigma-Aldrich, ACS reagent, ≥99.0% (KT)), (*ca* 61-292 nm) dispersed in a mixture of cyclohexane (Fisher Chemicals, 99%) and isobutylamine (Sigma-Aldrich, 99%) [6]. (See section SI.01 in the Supporting Information (SI) for transmission electron microscopy (TEM) analysis of the particles and their size distribution, and SI.02 for ZnO nano/microfluid preparation.) The surface pattern was created by casting a droplet (see SI.04 for details on procedures and conditions) onto a 1 × 1 cm silicon wafer (UV/Ozone treated, water contact angle (CA) = 10.3 ± 2.7°, in-house synthesised ZnO nanofluid CA = 6.5 ± 2.2°, ZnO nanopowder nano/microfluid CA = 5.5 ± 2.0°, and ZnO powder nano/microfluid CA = 4.1 ± 1.9° with the errors quoted as the standard deviation from 56, 28, 35, and 6 separate measurements, respectively). The surface patterns were characterised using scanning electron microscopy (SEM,

SI.05). The size distribution of the BM convective cells in the residual surface patterns structure was fitted with the log-normal distribution function (SI.06). Box counting fractal dimension analysis was used to further study images of manifestations of the BM cellular pattern (SI.07) to yield their fractal dimensions as a quantitative measure on these complex cells.

**Figure 1** shows examples of the residual surface patterns from evaporation of the droplets of the three types of particle dispersions. The pattern was composed of central cellular structures surrounded by a coffee ring band around the pinned droplet perimeter (**Figure 1a**, **d** and **g**), made of a dense network of intercalating fibres (**Figure 1b**-**c**, **e**-**f**, and **h**-**i**). For the in-house synthesised ZnO nanofluid, the central cells were approximately circular in shape with varying diameters (200 - 800 μm), with their microstructure resembling spoke-like patterns with a bow-tie projection (**Figure 1b**). The BM cell size distributions (**Figure 2**) were fitted with a log-normal function (SI.06) where *M* is the geometric mean BM cell size by count and $\sigma_g$ is the geometric standard deviation [16-17]. One of the well-defined cells is shown in **Figure 1c**. These cells, similar to the BM flow pattern observed during the evaporation of polystyrene/toluene solution [14], were identified as solidified manifestations of Bénard-Marangoni (BM) convection cells [3]. The occurrence of the BM instabilities and flows may be gauged by the Marangoni number, *B*, which considers the counter balancing effects of the surface tension and the viscous force in a liquid film [18], and it also depends on solvent physical parameters such as thermal diffusivity, dynamic viscosity, temperature gradient, thermal conductivity, density, and specific heat capacity. For $B > 80$, spontaneous surface-tension driven flows will result in BM instabilities and the formation of BM flow cells. The BM cell size in the residual pattern, $\lambda_{BM}$ is related to the Marangoni number by $B = 32(\pi d/\lambda_{BM})^2$, where *d* is the drop thickness [3]. Wu and Briscoe calculated that the Marangoni numbers in their evaporating ZnO nanofluid droplet (in a mixture of chloroform, methanol and isobutylamine) were $B \sim 300 - 2000$, much larger than the critical value of 80 [3]. They attributed different BM cell sizes to the fluctuations in the local fluid viscosity induced by the variation in the local particle concentration during the evaporation. Here, the varying BM cell sizes $\lambda_{BM}$ ~ 200 - 800 μm suggest that the BM flows were triggered at different droplet thickness *d* or thinning stages during the evaporation, which may be attributed to the inhomogeneities in the concentration of particle and molecular species *in situ* generated from ZnO dissolution [3, 5].

In contrast, drying of the nano/microfluid droplets from the commercially acquired ZnO nanopowder (**Figure 1d**-**f)** and ZnO powder (**Figure 1g**-**i)** left the substrate surface covered with dense, fibrous structures intercalated with ZnO nano/microcrystal residues, as shown in the insets in **Figure 1f** and **i**. This was attributed to ZnO crystals undergoing partial moisture-assisted dissolution over the course of evaporation, described in detail in [6]. These undissolved ZnO nano/microcrystals

could have influenced the solvent flows during the evaporation and contributed to the fluid viscosity fluctuations causing the BM instabilities. The BM cells in the residual pattern were less well-defined, with some of the spoke-like radial patterns outlined with yellow circles in the figure, showing dendritic morphologies with fibres radiating from the centre, with the BM cell size distributions shown in **Figure 2b** and **c**.

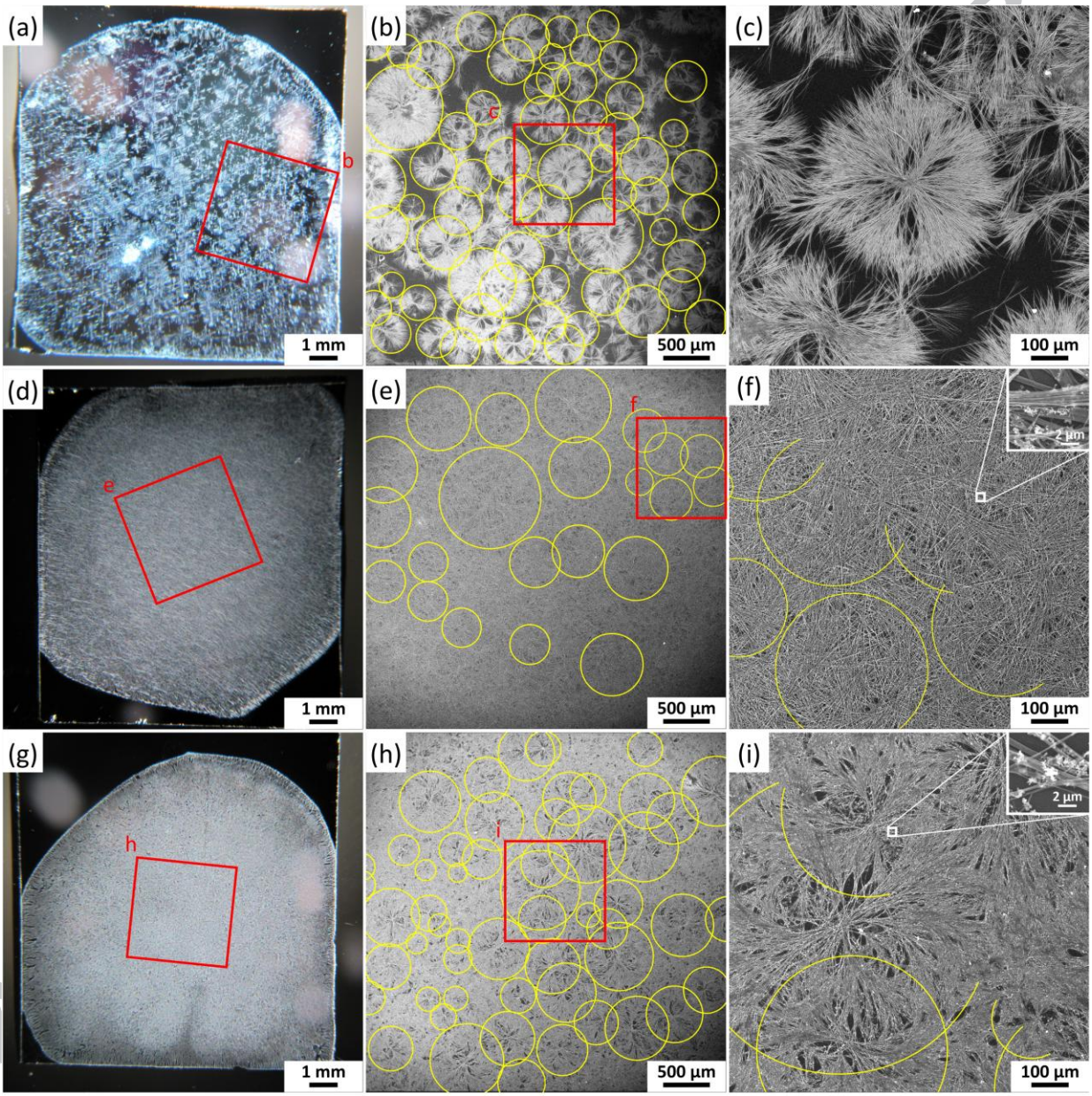


**Figure 1**. Residual surface pattern formed on the UV/Ozone treated silicon wafer from a 30 µL sessile droplet of the in-house synthesised ZnO nanofluid (**a**-**c**) and commercially acquired ZnO nanopowder (**d**-**f**) and ZnO powder (**g**-**i**) nano/microfluids; optical (**a**, **d** and **g**) and (**b**-**c**, **e**-**f** and **h**-**i**) scanning electron microscopy images. BM cells are marked with yellow circles, shown only for half of the micrographs in (**f**) and (**i**) for clarity. Insets if (**f**) and (**i**) show magnified views of the areas marked with white squares in the images, which reveal ZnO crystalline residues intercalating with fibres.

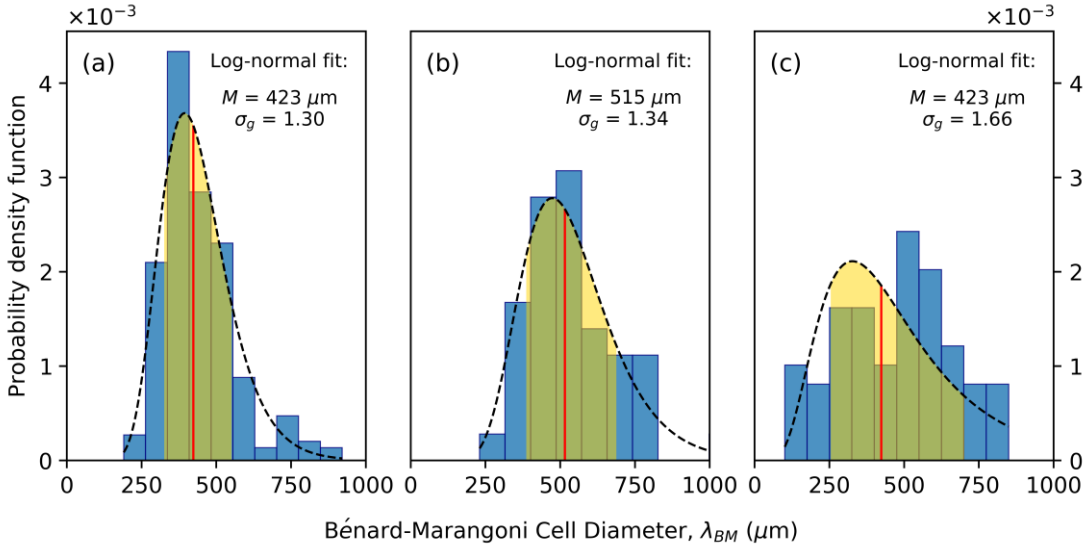


**Figure 2**. Size distributions as the probability density function (PDF) of BM cells in the central region of the residual surface patterns from (**a**) the in-house synthesised ZnO nanoparticles, and commercially acquired (**b**) ZnO nanopowder and (**c**) ZnO powder on UV/Ozone exposed silicon wafer. BM cell sizes distributions were fitted with a log-normal function (SI.06), shown as dashed lines. Red vertical lines show the geometric mean, $M$ (equal to median size in log-norm distribution). BM cells of sizes contained between $M/\sigma_g$ and $M \cdot \sigma_g$ (68.3% of all values) are shaded in golden colour under the dashed size distribution curve.

The box counting fractal dimension (FD) analysis was performed for individual BM cells and the process is described in detail in the supplementary information (SI.07). Briefly, BM cells of different diameters $\lambda_{BM}$ are identified by circles and the FD analysis is performed for each encircled area. The algorithm for the analysis involves laying a grid of square boxes of a side-length $\varepsilon$ over an image, and then counting the number of non-empty boxes, $N(\varepsilon)$, which scales with the box size $N(\varepsilon) \sim \varepsilon^{-D}$ (equation S5). The procedure is then repeated for a range of $\varepsilon$ to obtain the fractal dimension (FD), $D$, from the slope of the $\ln(N)$ vs. $\ln(\varepsilon)$ plot (equation S6) [10, 19]. The process is shown in **Figure 3** for the analysis of a single BM cell (cf. **Figure 1c**). As a control, the FD analysis was similarly performed for the whole image instead of individual BM cells.

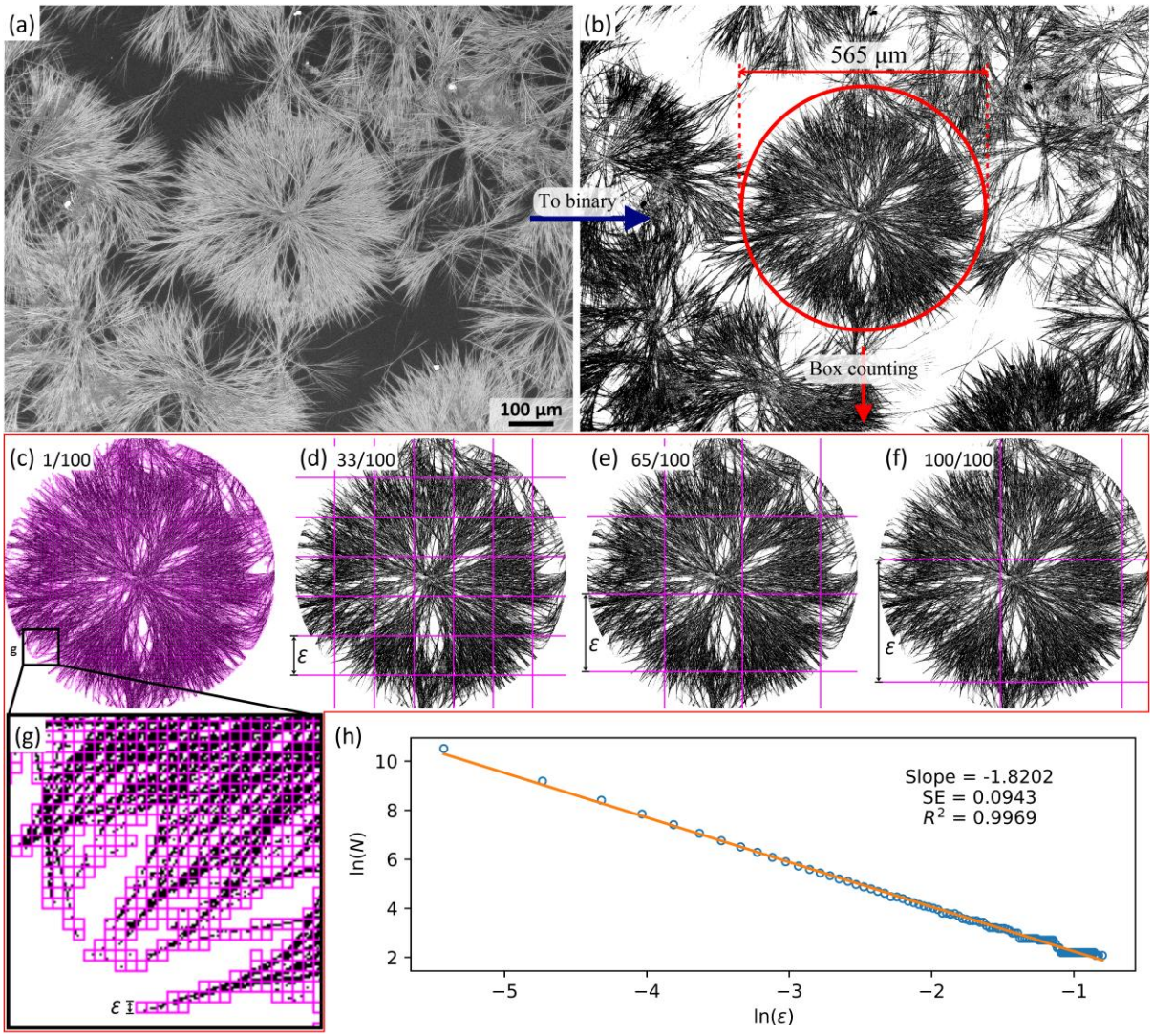


**Figure 3**. Step-by-step scheme of box counting fractal dimension (FD) analysis. An SEM image (**a**) is converted to binary form (**b**). Then, a circular selection concentric with a Bénard-Marangoni (BM) cell is analysed by superimposing a series of square grids of a box sampling size $\varepsilon$ on the image, and the number of boxes containing foreground pixels, $N$, is counted for each $\varepsilon$ (size 5, 165, 325, and 508 pixels for **c**-**f** respectively). The box counting FD is the negative slope of the best line fit to ln($N$) vs. ln($\varepsilon$) plot (**h**). SE stands for the standard error and $R^2$ for the correlation.

The results of the box counting FD analysis of the solidified BM cells are presented in **Figure 4**, with the $D$ values in the range 1.76 – 1.89. A fractal dimension can be used to gauge the geometrical properties of a structure, *e.g.* how much space it fills or how pronounced its irregularities are [20]. It can also be used to quantify ruggedness of particle boundaries [21]. The $D$ value distribution calculated as probability density function (PDF) is shown in **Figure 4a**, with the fitted the normal distributions also shown as black dashed lines and labelled as $h_1$, $h_2$ and $h_3$ for three types of ZnO nano/microfluids. The fitting parameters, $\mu$ and $\sigma$, stand for the mean $D$ value and its standard

deviation, respectively. The BM cells from the in-house ZnO nanofluid had the lowest average *D* value of $\mu$ = 1.822 with a broad distribution ($\sigma$ = 0.025). The BM cells from the other two types of ZnO particles ($h_2$ and $h_3$) showed a similar, higher average *D* value of $\mu$ ~ 1.84, consistent with a denser structure and a higher surface coverage. Numerically, such values compare to those for the classical fractals, *e.g.* *D* ≈ 1.8687 for both monkey trees and snowflake halls, and *D* = 1.8928 for the Sierpiński carpet [9]. For reference, a line gives a value of *D* = 1 and a fully filled area *D* = 2. The scatter in *D* values is qualitatively consistent with our interpretation on a physical level that the BM cell size variations were due to local inhomogeneities in the viscosity and thermal properties, with the larger BM cells resulting from the instabilities triggered at larger droplet thicknesses. The different flow rates and particulate species participating in the self-assembly process in different BM flow cells would lead to different fractal dimensions *D*. Furthermore, self-similarity is a measure how the pattern of the entire shape is similar to the pattern of an arbitrary small part of the shape. It can be expressed with the Hurst exponent, *H* = 2 - FD, for a 2D pattern [22]. The values of the Hurst exponent for all the patterns are *H* < 0.5, which lie in the region of unstable statistical characteristics. For instance, in computer aided cancer diagnosis of magnetic resonance images, this usually suggests that the physiological pattern is related to a pathological condition in contrast to a stable statistical region of *H* > 0.5.

A trend of increasing FD values (*D*) vs. the BM cell diameter ($\lambda_{BM}$) may also be observed (**Figure 4b**) for all the nano/microfluids, initially a rapid increase in *D* for small BM cell diameters ($\lambda_{BM}$ < 200-400 μm), but reaching a plateau for higher $\lambda_{BM}$ values. A logarithmic function was loosely fitted to the trend, $D = a\ln(\lambda_{BM}) + D_0$, with the intercept value $D_0$ for the in-house synthesised ZnO nanofluids the smallest *ca* 1.538 compared to those for the other two types ($D_0$ = 1.708 and 1.736 respectively). This could be attributed to the voids (*i.e.* unoccupied areas) towards the centre of the dendritic pattern, giving rise to a smaller $D_0$ value, characteristic of a fractal pattern with a less densely populated area. The scatter in the data for different particles is enclosed in respective shaded areas bounded also by the logarithmic fits (Section SI.07 in SI). It should be noted (and as discussed in SI.07) that the choice of the logarithmic function is arbitrary which merely provides a guidance to the eye. It however facilitates an internally consistent comparison between the three sets of FD values.

A benchmark FD analysis was also performed on two known fractal structures, a hexaflake and the Sierpiński carpet (**Figure S3**), using the circles of different diameters (as we did for the different BM cell sizes above). A similar trend of rapid increase in *D* followed by a plateau was also observed as for the BM cells, again with smaller intercept values $D_0$ for the patterns with a more open structure in the centre. A series of circular selections of different diameters (in the rage of 8.7% to

62.3% of the largest diameter analysed) that covered a random part of the Sierpiński carpet, instead of being concentrically symmetric with the fractal pattern, were also processed. The *D* values scattered around the average value ($\mu$ = 1.75 and $\sigma$ = 0.02; **Figure S3b**), without the depressed *D* values at smaller circle diameters. This is due to the random placements of the circles which averaged out the less densely packed area close to the centre of the fractal patterns, further confirming the origin of the observed the *D* vs. $\lambda_{BM}$ trend in Figure 4b. To appreciate its physical significance, we may draw an analogy between the BM cell dendrites with the polymeric dendrimers smaller (or lower generation) dendrimers possess a more open structure, whilst larger (or higher generation) dendrimers have a much denser packing [23-24].

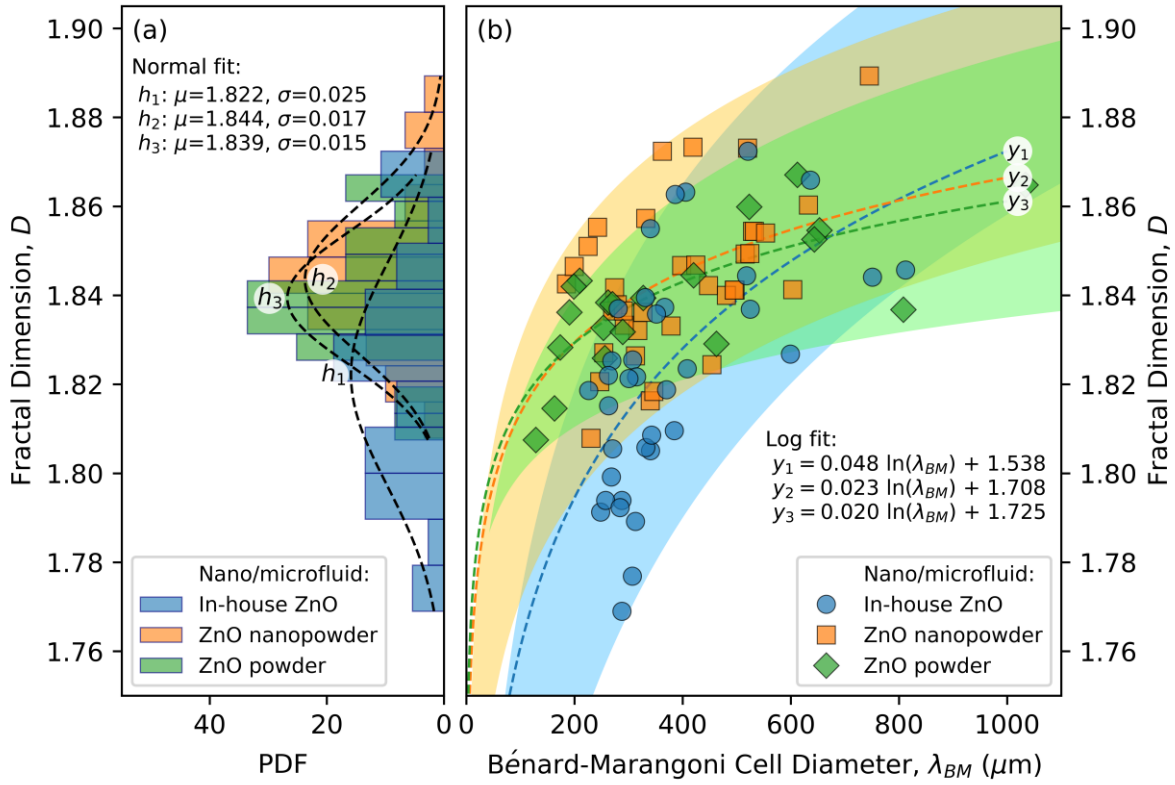


**Figure 4**. Box counting fractal dimension analysis of the solidified Bénard-Marangoni (BM) cells from drying ZnO nano/microfluids composed the in-house synthesised ZnO nanoparticles, ZnO nanopowder, and ZnO powder on a UV/Ozone exposed silicon wafer. (**a**) FD distribution for all the samples, fitted with normal (Gaussian) distribution function. Data fits are shown as dashed lines and labelled as $h_1$, $h_2$ and $h_3$, respectively for the three particle types. Parameters $\mu$ and $\sigma$ stand for the mean *D* and its standard deviation. (**b**) The calculated box counting fractal dimension (FD) vs. the diameter of the investigated BM cell $\lambda_{BM}$. Dashed lines, labelled $y_1$, $y_2$ and $y_3$, show logarithmic fits. The scatter of the data is enclosed by shaded regions, bounded also by the logarithmic fits (Section SI.07 in SI).

The residual surface patterns formed from ZnO nano/microfluids resembled the structures from diffusion-limited aggregation (DLA) [14, 25-26], and such particle aggregation has been simulated on square lattices (Euclidean dimensions equal to 2). These simulations resulted in branching patterns with a fractal (density correlation) dimension $D$ ~ 1.70. However, Bensimon *et al.* [27] modified the approach presented in [14, 26], assuming that the aggregation could be described by ballistic motion of the incoming particles joining the aggregate. The consequent DLA patterns resulted in a fractal dimension $D$ ~ 1.93 ± 0.02. Daccord and Lenormand [15] analysed the patterns obtained from chemical dissolution resembling tree-like structures and obtained a fractal dimension $D$ ~ 1.6 ± 0.1. It is worth mentioning that in addition to analysing circular selection of patterns resembling solidified manifestations of BM cells from ZnO nano/microfluids, the whole SEM images that were used for BM cells analysis were also processed (**Table S3**). The FD values calculated for the whole SEM images follow a similar trend to that observed for the BM cells, with the smallest $D$ value obtained for the in-house ZnO nanofluid (1.896 ± 0.001, for $\mu$ and $\sigma$, respectively), with the rest of the patterns resulting in $D$ ~ 1.908 ± 0.007 (ZnO powder nano/microfluid) and 1.911 ± 0.006 (ZnO nanopowder nano/microfluid). This is with agreement to the work of Daccord and Lenormand [15], also providing further supporting evidence for the discussion in Ref. [3] that the dendritic patterns are produced in a DLA process. However, one should note different methods for fractal dimension calculation may result in slightly different values of fractal dimensions for the same structure, depending on the dimension definition [20].

In summary, we have presented a fractal dimension analysis of the solidified Bénard-Marangoni cells of complex morphology in the residual surface patterns from evaporation of sessile drops containing different ZnO nano/microfluids. Such an analysis facilitates discussions of the features and properties of the surface patterns beyond the previous descriptive account [3, 5-6]. The fractal dimension $D$ value reflects the ruggedness or how much space the dendritic pattern fills [20-21], whilst the $D$ vs. $\lambda_{BM}$ (BM cell size) trend and the intercept value $D_0$ of its logarithmic fit give insights into the spatial variation of the dendrites from the BM cell centre to its periphery. ZnO nanofluids prepared from the commercially acquired ZnO nanopowder and ZnO powder produced patterns of a higher coverage with densely packed BM cells and a higher degree of interpenetration between them, manifesting in higher values of the fractal dimension. Our results demonstrate that fractal dimensional analysis can provide a quantitative description of the properties of these complex surface patterns from evaporative drying of reactive nanofluids, which paves the way for further investigations to seek further correlation between the fractal dimensions and the physical parameters relevant to the evaporation process and solution conditions. For instance, we have applied the fractal dimension analysis developed here to investigate the effect of substrate

chemistry on the residue patterns (Wasik *et al.* in preparation). Our results also point to the feasibility for such an analysis for other similar quai-2D surface patterns.

**Supporting Information**

The Supporting Information (SI) associated with this article can be found, in the online version, at https://doi.org/XXX. The SI contains: SI.01: ZnO particles; SI.02: Preparation of the nano/microfluids; SI.03: Preparation of the substrates; SI.04: Hierarchal surface pattern formation; SI.05: Characterisation of the hierarchical surface patterns; SI.06: Bénard-Marangoni cell size distribution - log-normal fitting; and SI.07: Fractal dimension analysis of the Bénard-Marangoni cells.

**ORCID**

Patryk Wąsik - 0000-0002-7447-7472

Annela M. Seddon - 0000-0002-5794-8500

Wuge H. Briscoe - 0000-0001-8025-960X

**Acknowledgements**

P.W. is supported by the UK Engineering and Physical Sciences Research Council (EPSRC) through the Bristol Centre for Functional Nanomaterials (BCFN) (grant no. 1371498). H.W. is supported by a Marie Skłodowska-Curie Individual Fellowship (Project Number 656830). W.H.B. would like to acknowledge funding from the EPSRC (EP/H034862/1 and Building Global Engagement in Research (BGER)), European Cooperation in Science and Technology (CMST COST) Action CM1101 “Colloidal Aspects of Nanoscience for Innovative Processes and Materials”, and Marie Curie Initial Training Network (MCITN) on “Soft, Small, and Smart: Design, Assembly, and Dynamics of Novel Nanoparticles for Novel Industrial Applications” (NanoS3). Mr Jonathan Jones and Dr Sean Davis are thanked for their help with SEM imaging. Ms Anna Slastanova is acknowledged for her help with the contact angle measurements. Ms Kate Oliver is thanked for a discussion about the approach to the fractal dimension analysis of digital images.

**References**

1. Han, W.; Lin, Z., Learning from “Coffee Rings”: Ordered Structures Enabled by Controlled Evaporative Self-Assembly. *Angew. Chem. Int. Ed.* **2012,** *51* (7), 1534-1546.

2. Zhong, X.; Crivoi, A.; Duan, F., Sessile nanofluid droplet drying. *Adv. Colloid Interface Sci.* **2015,** *217*, 13-30.

3. Wu, H.; Briscoe, W. H., Morphogenesis of polycrystalline dendritic patterns from evaporation of a reactive nanofluid sessile drop. *Physical Review Materials* **2018,** *2* (4), 045601.

4. Deegan, R. D.; Bakajin, O.; Dupont, T. F.; Huber, G.; Nagel, S. R.; Witten, T. A., Capillary flow as the cause of ring stains from dried liquid drops. *Nature* **1997,** *389* (6653), 827-829.

5. Wu, H.; Chen, L. X.; Zeng, X. Q.; Ren, T. H.; Briscoe, W. H., Self-assembly in an evaporating nanofluid droplet: rapid transformation of nanorods into 3D fibre network structures. *Soft Matter* **2014,** *10* (29), 5243-5248.

6. Wąsik, P.; Redeker, C.; Dane, T. G.; Seddon, A. M.; Wu, H.; Briscoe, W. H., Hierarchical Surface Patterns upon Evaporation of a ZnO Nanofluid Droplet: Effect of Particle Morphology. *Langmuir* **2018,** *34* (4), 1645-1654.

7. Maroto, J. A.; Pérez-Muñuzuri, V.; Romero-Cano, M. S., Introductory analysis of Bénard–Marangoni convection. *European Journal of Physics* **2007,** *28* (2), 311.

8. Bénard, H., Étude expérimentale des courants de convection dans une nappe liquide. — Régime permanent : tourbillons cellulaires. *J. Phys. Theor. Appl.* **1900,** *9* (1), 513-524.

9. Mandelbrot, B. B., *The Fractal Geometry of Nature*. 1982.

10. Alligood, K. T.; Sauer, T. D.; Yorke, J. A., *Chaos: An Introduction to Dynamical Systems*. Springer New York: 2012.

11. Mandelbrot, B., How Long Is the Coast of Britain? Statistical Self-Similarity and Fractional Dimension. *Science* **1967,** *156* (3775), 636-638.

12. Masters, B. R., Fractal Analysis of the Vascular Tree in the Human Retina. *Annual Review of Biomedical Engineering* **2004,** *6* (1), 427-452.

13. Baish, J. W.; Jain, R. K., Fractals and Cancer. *Cancer Research* **2000,** *60* (14), 3683-3688.

14. Witten, T. A.; Sander, L. M., Diffusion-Limited Aggregation, a Kinetic Critical Phenomenon. *Phys. Rev. Lett.* **1981,** *47* (19), 1400-1403.

15. Daccord, G.; Lenormand, R., Fractal patterns from chemical dissolution. *Nature* **1987,** *325*, 41.

16. Smith, J. E.; Jordan, M. L., Mathematical and graphical interpretation of the log-normal law for particle size distribution analysis. *J. Colloid Sci.* **1964,** *19* (6), 549-559.

17. Zender, C. Particle size distributions: theory and application to aerosols, clouds, and soils. http://dust.ess.uci.edu/facts/psd/psd.pdf (accessed 12th Dec 2017).

18. Pearson, J. R. A., On convection cells induced by surface tension. *J. Fluid Mech.* **1958,** *4* (5), 489-500.

19. Napolitano, A.; Ungania, S.; Cannata, V., Fractal Dimension Estimation Methods for Biomedical Images. In *MATLAB - A Fundamental Tool for Scientific Computing and Engineering Applications - Volume 3*, Katsikis, V. N., Ed. InTech: Rijeka, 2012; p Ch. 07.

20. Falconer, K. J., *Fractal geometry: mathematical foundations and applications*. Wiley: 1990.

21. Rahman, M. S., Physical meaning and interpretation of fractal dimensions of fine particles measured by different methods. *J. Food Eng.* **1997,** *32* (4), 447-456.

22. Marusina, M. Y.; Mochalina, A. P.; Frolova, E. P.; Satikov, V. I.; Barchuk, A. A.; Kuznetcov, V. I.; Gaidukov, V. S.; Tarakanov, S. A., MRI Image Processing Based on Fractal Analysis. *Asian Pacific Journal of Cancer Prevention : APJCP* **2017,** *18* (1), 51-55.

23. Pilkington, G. A.; Pedersen, J. S.; Briscoe, W. H., Dendrimer Nanofluids in the Concentrated Regime: From Polymer Melts to Soft Spheres. *Langmuir* **2015,** *31* (11), 3333-3342.

24. Fox, L. J.; Richardson, R. M.; Briscoe, W. H., PAMAM dendrimer - cell membrane interactions. *Adv. Colloid Interface Sci.* **2018,** *257*, 1-18.

25. Witten, T. A.; Meakin, P., Diffusion-limited aggregation at multiple growth sites. *Physical Review B* **1983,** *28* (10), 5632-5642.

26. Meakin, P., Diffusion-controlled cluster formation in 2\char22{}6-dimensional space. *Physical Review A* **1983,** *27* (3), 1495-1507.

27. Bensimon, D.; Domany, E.; Aharony, A., Crossover of Fractal Dimension in Diffusion-Limited Aggregates. *Phys. Rev. Lett.* **1983,** *51* (15), 1394-1394.

Graphical abstract